International Journal of Nanomedicine

Dovepress

open access to scientific and medical research

Open Access Full Text Article

ORIGINAL RESEARCH

Cell Membrane Coated pH-Responsive Intelligent Bionic Delivery Nanoplatform for Active Targeting in Photothermal Therapy

Xiangyu Zhang[1], Zelai He[2]

[1]Department of Pathology, Jining No.1 People's Hospital, Jining, Shandong, 272000, People's Republic of China; [2]Department of Radiation Oncology, the First Affiliated Hospital of Bengbu Medical College & Tumor Hospital Affiliated to Bengbu Medical College, Bengbu, Anhui, 233004, People's Republic of China

Correspondence: Zelai He, Department of Radiation Oncology, The First Affiliated Hospital of Bengbu Medical College & Tumor Hospital Affiliated to Bengbu Medical College, Bengbu, 233004, People's Republic of China, Email he.ze.lai@163.com

Aim: To produce pH-responsive bionic high photothermal conversion nanoparticles actively targeting tumors for sensitizing photothermal therapy (PTT).

Materials and Methods: The bionic nanoparticles (ICG-PEI@HM NPs) were prepared by electrostatic adsorption of indocyanine green (ICG) coupled to polyethyleneimine (PEI) and modified with tumor cell membranes. In vitro and in vivo experiments were conducted to investigate the efficacy of ICG-PEI@HM-mediated PTT.

Results: The intelligent responsiveness of ICG-PEI@HM to pH promoted the accumulation of ICG and enhanced the PTT performance of ICG-PEI@HM NPs. Compared with free ICG, NPs exhibited great photothermal stability, cellular uptake, and active tumor targeting for PTT.

Conclusion: ICG-PEI@HM NPs can enhance the efficacy of PTT and can be used as a new strategy for the construction of photothermal agents.

Keywords: photothermal therapy, pH-responsive, tumor membrane, active targeting, nanoparticle

Introduction

Light-mediated photothermal therapy (PTT) and photodynamic therapy (PDT) have attracted significant attention for tumor treatment in recent years for their minimal invasiveness, site-specific activation and proven clinical applications.[1,2] PDT disrupts tumor cells by generating large amounts of reactive oxygen species (ROS) in the presence of near-infrared light through a photosensitizer.[3] Similarly, PTT employs photothermal conversion agents to convert light energy into heat energy above tumor tolerance level and produces ROS to kill tumor cells, ROS was produced mainly through the damaged mitochondria.[4,5] Comparatively, PTT is rapid and more effective. However, inhomogeneity and inefficient conversion efficiency of light energy require better photothermal agents (PTAs) that are available to further enhance the efficiency of PTT.[5]

Conventional PTAs, such as gold nanoparticles (NPs) and graphene, have demonstrated adequate photothermal conversion efficiency. Among them, nano-scale drugs have increased permeability and retention (EPR) effects and preferentially accumulate drugs in tumors. However, the efficacy of passively targeted nanomedicine is not always satisfactory, as it is largely influenced by the heterogeneity of the intensity of EPR effects between tumors at different growth stages.[6] As a result, photothermal conversion nanoparticles often limit the efficacy of PTT due to lack of targeting, in addition to the pitfalls of biotoxicity in the therapeutic pathway. Increasingly, targeting strategies are being introduced into the design of PTAs to sensitize PTT. Thus, new strategies are required to enhance their antitumor effect. NPs designed with ligand receptors for tumor targeting have the risk of off-targeting and low immune compatibility, while nanomaterials modified with hyaluronic acid or other chemicals have problems of macrophage clearance.[7]

Received: 24 August 2023
Accepted: 29 November 2023
Published: 15 December 2023

Researchers have now reported a biomimetic strategy for constructing cell membrane encapsulated high-affinity nanomaterials.[8,9] Furthermore, it has been shown that erythrocyte membrane encapsulated quantum dot particles not only resist the hypoxic microenvironment of tumor lesions but also show better biosafety.[9] Compared to normal cell membranes, NPs camouflaged with tumor cell membranes exhibited better activity targeting. In addition, bionic NPs overcome self-clearance greatly increasing drug retention at the target site. And the therapeutic effect was effectively enhanced.[8] Overall, bionic modification using cancer cell membrane may be the best strategy for constructing targeted PTAs.[10]

Indocyanine green (ICG), an anthocyanin compound, exhibits fluorescence properties in the Near-infrared (NIR) region.[11] ICG imaging can be used for intraoperative differentiation of solid tumors, metastases, and sentinel lymph nodes.[12] In addition, it can be employed as a PTA for the destruction of malignant tissues via the production of ROS and/or heat induced by irradiation. However, inferior water solubility and rapid metabolism have restricted the clinical application of ICG. Nanodrug delivery systems using ICG as a carrier have improved the therapeutic efficacy of ICG by improving its stability, biodistribution and accumulation at the tumor site. Zhou et al designed a novel nanoplatform (TiO_2:Yb, Ho, F-β-CD@ICG/HA) for NIR-induced phototherapy as well as multimode imaging (UCL/MRI/Flu), which prevented ICG aggregation and enhanced its stability.[13] The outstanding antitumor outcomes of ICG highlight the demand for nanocarrier design. Studies have previously reported that highly biocompatible nanocarriers, such as transferrin and human serum albumin (HSA) can effectively transport ICG and overcome early drug leakage to improve antitumor efficiency.[14] Beyond bionic modifications that can improve the antitumor efficiency of PTAs, smart responsive PTA materials may increase the accuracy of PTT.[15]

Therefore, in the current study, we engineered pH-responsive smart-targeted biomimetic nanoparticles for effective synergistic PTT against tumors (Figure 1). In this study, we constructed the biomimetic nanomaterial ICG-PEI@HM by using tumor cell membrane as nanocarriers and Polyethyleneimine (PEI) coupled ICG as PTA. Importantly, the benzoic acid-imine bond between ICG and PEI is acidifiable. Once the ICG-PEI@HM reaches the lesion through the tumor-targeting action of the H1975 cell membrane, the composite nanomaterial is rapidly disintegrated by the breakage of benzoic acid-imine bond, which provokes the release of ICG and affords deep tumor penetration. In addition, the photothermal conversion efficiency of ICG is promoted by exploiting the high penetration effect of the drug. Mechanistically, the NPs generate a large number of ROS at the target site, effectively inhibiting the proliferation of tumor cells. Such intelligent bionanoplasmic nanoplatforms could have a broad range of clinical applications.

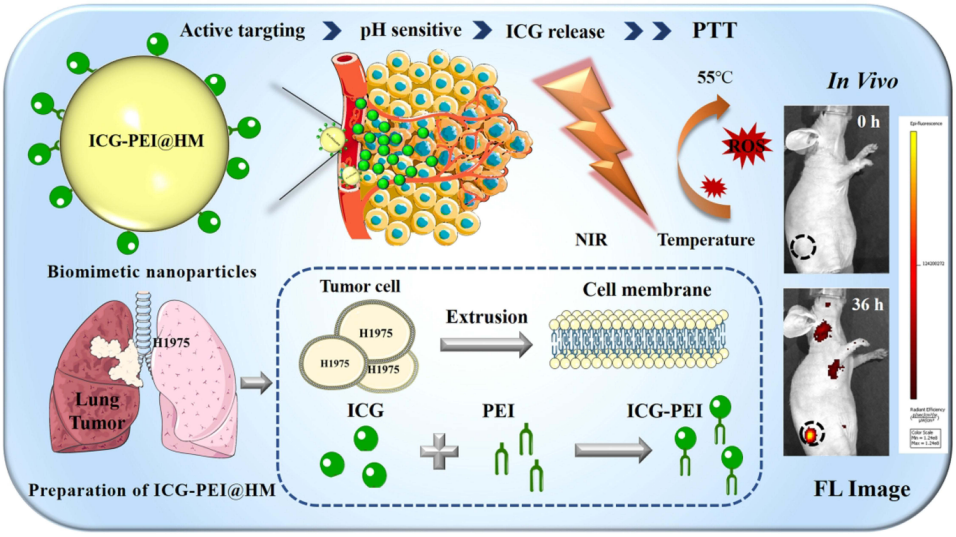

Figure 1 Schematic design and preparation of ICG-PEI@HM NPs for PTT strategy.
Abbreviations: ICG, Indocyanine green; PEI, Polyethyleneimine; HM, H1975 cell membrane; FL, Fluorescence; PTT, Photothermal therapy; NPs, Nanoparticles.

Materials and Methods

Materials and Cell Line

ICG, PEI (Mn=2500), and Polyethylene glycol (Mn = 4000) were obtained from Sigma-Aldrich (St Louis, MO, USA). 2′,7′-dichlorofluorescin diacetate (DCFH-DA), 4',6-diamidino-2-phenylindole (DAPI), 3-(4, 5-dimethyl-2-thiazolyl)-2, 5-diphenyl-2-H tetrazolium bromide (MTT), bicinchoninic acid protein kit (BCA), TUNEL apoptosis detection kit, Calcein AM/PI (propidium iodide) kit, and Trypsin EDTA were purchased from Beyotime Biotechnology (China). Dulbecco's modified Eagle's medium (DMEM, high-glucose) and FBS were acquired from Gibco Life Technologies (AG, USA). The dimethyl sulfoxide (DMSO), ethanol, and other reagents were obtained from Aladdin Co., Ltd (China). Both dialysis bags (MW=1000 Da & MW=3500 Da) were purchased from Solarbio Life Sciences (China).

H1975 cells, NIH-3T3 cells were purchased from Cell Resource Centre, Institute of Basic Medical Sciences, Chinese Academy of Medical Sciences, China.

Preparation of Tumor Membranes

The synthesis of preparing the cell membrane was referred to the study by Zhang et al.[8] The H1975 cells in the logarithmic growth phase were digested to collect cell clumps (counted as 1×10^8). Then, the cells were resuspended in 1 mL of pre-chilled buffer (TM buffer, 0.01 M Tris) with protease inhibitors and 0.001 M $MgCl_2$ (pH 7.4). The cell suspension was ultrasonicated for 2 min using an ultrasonic disintegrator (duty ratio 20%) and then placed on ice for 35 min with shaking. The cells were damaged with an extrusion device using mechanical squeezing for 10 cycles. The obtained cell solution was collected and added with an appropriate amount of sucrose solution (prepared in TM buffer, 1 M) for a final sucrose concentration of 0.25 M. To remove intracellular material, the mixture was centrifuged at 4°C and 2000 g for 10 min. The collected supernatant was subjected to high-speed centrifugation at 4°C and 15,000 g for 30 min. Finally, the crumb was resuspended in pre-cooled phosphate buffer solution (1× PBS), using mild ultrasonication for 2 min; this is the final cell membrane product. Lastly, the BCA assay was used for protein concentration estimation of the extracted product.

Synthesis of ICG-PEI & ICG-PEI@HM NPs & ICG Standard Curve

Firstly, the ICG probe (0.01 mg) was dissolved in 2 mL of anhydrous methanol to obtain the mother liquor by magnetic stirring for 15 min. An appropriate amount of PEI was dispersed in deionized water to prepare the mother liquor (5 mg/mL). Then, 10 μL of ICG was dispersed in deionized water and PEI (25% w/w) was added with continuous stirring for 4 h. After the reaction completion, the ICG-PEI NPs were collected and stored in Eppendorf tubes at 4°C in the dark.

The extracted H1975 cell membranes were added to ICG-PEI solution. Air bubbles as well were removed. And the mixture was repeatedly extruded (15 times) with an extruder equipped with 200 and 100 nm polycarbonate membranes to obtain ICG-PEI@HM NPs. To remove unloaded ICG and protein, ICG-PEI@HM were subjected to 12 h of dialysis at 4°C in the dark.

The ICG powder was weighed and dissolved in anhydrous methanol, and different concentrations of ICG were prepared based on gradient dilution (0 μg/mL, 20 μg/mL, 40 μg/mL, 60 μg/mL, 80 μg/mL, 100 μg/mL, 150 μg/mL, 300 μg/mL, 600 μg/mL). 0.2 mL of each group of free ICG was then measured for absorbance values (OD=798 nm). The relationship between free ICG concentration and absorbance value was analyzed using Origin 8.5 software. And the standard curve was established to quantify the ICG content contained in the samples.

Characterization of ICG-PEI & ICG-PEI@HM NPs

For the negative electron staining, ICG-PEI@HM NPs were stained with 2% phosphotungstic acid dye solution for 15 min, followed by washing with deionized water to remove the background. Also, the morphology of NPs in different pH (6.8 or 7.4) media was observed under a transmission electron microscope (HT7700 Hitachi, Japan). The absorption and emission properties of the samples were analyzed using the SpectraMax M5 multifunctional microplate reader (Molecular Devices, US). Before particle size and zeta potential analysis (Nano ZS90 Zetasizer Nanoseries; Malvern

Instrument Ltd., UK), the samples were appropriately diluted with deionized water. ICG-PEI@HM dispersed in deionized water were analyzed for change in particle size for 30 days.

The Stability of ICG-PEI@HM NPs

ICG-PEI@HM were dispersed in PBS and deionized water for moderate dilution and the size changes of the NPs were recorded for 30 consecutive days. For thermal stability analysis, ICG-PEI@HM NPs were incubated in a 55°C constant temperature water bath for 240 min and the size of the material was measured every 30 min (in PBS) with a Nano ZS90 Zetasizer Nanoseries instrument.

pH-Responsive Drug Release

To evaluate the pH-triggered release profile of ICG-PEI@HM NPs, the in vitro release pattern of ICG from prodrug NPs was investigated at room temperature (RT) using 0.01 M PBS (pH 5.0, 6.0, 6.8, or 7.4) as the release medium. One milliliter of nanomaterials (containing ICG 1 mg/mL) were placed into a dialysis bag (MWCO=1kDa) to dialyze in 10 mL of release medium. 0.3 mL of release medium was withdrawn at certain time intervals (0, 2, 5, 10, 20, 30, 40, and 60 min) and the original release medium volume was maintained with an equal volume of fresh PBS. The collected-release medium samples were then analyzed for drug release rate using an enzyme marker and the control (pH 7.4).

In vitro Photothermal Properties of ICG-PEI@HM NPs

One milliliter of PBS, free ICG, PEI, and ICG-PEI@HM NPs were irradiated with 808 nm laser (1 W/cm^2) for 10 min, and the temperatures were recorded every 30s using a thermocouple thermometer and an infrared camera. Using an infrared thermographer, infrared thermograms were obtained for each group of samples after irradiation. In addition, 1 mg/mL of ICG-PEI@HM NPs were irradiated with different laser powers (0.2, 0.5, 1.0, and 1.5 W/cm^2) for 10 min and the temperature was recorded every 30s. η was calculated by the previous method.[16]

The measurement of the photothermal conversion efficiency (η) was calculated using the following equation based on the literature:[16]

h is the heat transfer coefficient, s is the surface area of the container, Q_{Dis} represents heat dissipated from the laser mediated by the solvent and container, I is the laser power, and A is the absorbance at 808 nm.

$$\eta = \frac{hs(T_{max} - T_{surr}) - Q_{Dis}}{I\left(1 - 10^{-A}808\right)}$$

m is the mass of the solution containing the photoactive material, C is the specific heat capacity of the solution, and τs is the associated time constant.

$$hs = \frac{mC}{\tau_s}$$

θ is a dimensionless parameter known as the driving force temperature.

$$\tau = -\tau_s \ln(\theta)$$

T_{max} is the maximum steady-state temperature and T_{Surr} is the environmental temperature.

$$\theta = \frac{T - T_{surr}}{T_{max} - T_{surr}}$$

ROS Generation

The ROS yield was assessed by the single-linear oxygen trap SOSG probe. First, SOSG powder was prepared a 5 mM mother liquor with methanol, followed by dilution with deionized water at a ratio of 1:1000. Then, 10 μL of ICG-PEI @HM was incubated with 0.5 mL of probe working solution for 15 min at different power intensities (0.5, 1.0, and 1.5 W/cm^2; 808 nm laser) and the samples were collected after 10 min. The fluorescence intensity of SOSG was detected with Spectrophotometer F7000 (Hitachi, Japan).

After binding to ROS, the fluorescence emitted by the DCFH-DA probe can reflect the ROS production of ICG-PEI@HM at the cellular level. Briefly, after ingestion of ICG-PEI@HM nanoparticles for 12 h, H1975 cells were incubated overnight at 37°C and 5% CO_2. Then DCFHDA (5 μM) was added and incubated for 1 h. Cells were irradiated with 808 nm laser (1 W/cm^2) for 10 min. After 0.5 h of stabilization, cells were stained with 4′,6-cytosine by 4′,6-diamidino-2-phenylindole (DAPI) for 10 min and finally analyzed by fluorescence microscopy (Leica, Germany) and flow cytometer (ACEA Biosciences Inc., USA) for image acquisition and fluorescence intensity quantification, respectively. ROS was mainly reflected by tissue sections in vivo. At first, the tumor-bearing mice were injected intravenously with ICG-PEI@HM NPs. These mice were randomly grouped and pH adjusted (6.8 or 7.4). DCFH-DA (5 μM) was then injected into the target site, and after laser irradiation of the mice (808 nm, 1 W/cm^2, 10 min), the tumors were removed within 4 h and serial frozen sections were performed. Finally, images were collected with fluorescence microscopy.

Cellular Uptake

H1975 cells were cultured overnight in DMEM high glycemic medium containing 10% fetal bovine serum (FBS) at 37°C and 5% CO_2. The medium was replaced with a fresh medium (pH 7.4 or 6.8) containing NPs or free ICG at 1 or 12 h, respectively. Cells were stained with DAPI for 10 min and observed with a laser confocal microscope (Leica, Germany). To further assess pH-triggered ICG-PEI@HM NPs, the fluorescence intensity of ICG-PEI@HM released intracellular ICG was quantified by flow cytometry using pH 7.4 conditioned culture group as a control.

The targeting of ICG-PEI@HM NPs was assessed based on the cellular uptake behavior. Briefly, NPs were incubated with different cell lines, including bEnd.3, SW1990, C6, 4T1, and H1975 cells. 10^5 cells were placed in 500 μL of culture medium in 24-well plates. After 12 h of incubation, the cell medium was replaced with a fresh medium containing ICG-PEI@HM (ICG = 5 μg/mL). After another 4 h, the cell suspensions were collected after washing with PBS for flow cytometry analysis. In addition, we also examined the uptake of ICG-PEI NPs and ICG-PEI@HM NPs after 12 hours in H1975 cells. The details were consistent with the methods described above. And the results were finally detected by fluorescence microscopy and flow cytometry.

MTT Assay for Cell Viability

The potential cytotoxicity of ICG-PEI@HM NPs was assessed by MTT assay. NIH3T3 or H1975 cells were incubated overnight, followed by incubation with different concentrations of ICG-PEI@HM NPs for 12 h. The medium was replaced with a fresh medium containing MTT (20 μL) with 4 h incubation. Lastly, the medium was replaced with DMSO and cell viability was measured using an enzyme marker. The same method was also used to screen the effect of drug concentration with different optical power irradiation on tumor cell viability.

Calcein AM/PI Staining Assay for Drug Toxicity

To assess the toxicity of ICG-PEI@HM NPs, H1975 cells were inoculated in 96-well plates (1×10^4 cells per well, 100 μL medium) and incubated overnight. Then, the cells were treated with ICG-PEI@HM containing 5 μg/mL ICG. After incubation for 12 h, cells were irradiated with 808 nm laser (1 W/cm^2, 10 min) and incubated for another 4 h. Lastly, cells were respectively stained with Calcein AM and PI and then subjected to image collection using an inverted fluorescence microscope (Leica, Germany).

In vitro Tumor Tissue Drug Permeation

The drug permeation assays were performed on H1975 tumor tissues in vitro. Briefly, H1975 cells (2×10^7 cells/mL) were injected subcutaneously on the dorsal right side of a male BALB/c nude mouse (4 to 6 weeks old). Animals were monitored for tumor growth, and when tumors grew to 200 mm^3, tail vein injections of ICG-PEI@HM (ICG 0.5 mg/kg) at different pH values were moderately cycled for about 12 h. Mice were euthanized to obtain tumor tissues, which were processed by frozen sectioning. The sections located in the inner core of tumor tissues were subjected to DAPI staining and analyzed using a fluorescent body microscope (Zeiss, Germany).

In vivo Optical Imaging and Tissue Distribution

BALB/c nude mice loaded with H1975 tumors (200 mm^3) were injected intravenously with 200 μL ICG-PEI@HM NPs or free ICG (both at 0.5 mg/kg). The control mice were anesthetized at different time points (3, 6, 12, and 36 h after injection), and images were acquired using the IVIS imaging system (Xenogen, US). Mice were euthanized 36 h after injection to image major organs.

Antitumor Efficacy and Histological Analysis

Animal models were established by subcutaneous injection of H1975 cells (2×10^7 cells/mL) into the dorsal right side of male BALB/c nude mice (5 to 6 weeks old) to grow tumors up to 200 mm^3 diameter. Mice were randomly divided into five groups (n = 9), namely the Control, ICG-PEI@HM, ICG+Laser, ICG-PEI+Laser, and ICG-PEI@HM+Laser groups. Each group was intravenously injected with the nanodrug containing ICG (0.5 mg/kg), while the mice of Light groups were also treated with laser irradiation (808 nm, 1 W/cm^2, 10 min) after 12 h interval. Mice's body weight and tumor size (long and wide axes) were measured and recorded daily. Within 72 h of treatment, from each group, tumor tissues from three mice were washed with saline, fixed in 10% formalin, and then embedded in paraffin blocks for sectioning and staining with hematoxylin and eosin (H&E). The remaining mice were observed for 21 days. At the end of the monitoring period, animal blood was collected and allowed to clot. Samples were centrifuged at 3500 rpm for 10 min to obtain serum for liver and kidney function analysis. The major animal organs (heart, liver, spleen, lung, and kidney) were embedded and fixed as described above, and the sections were stained for observation.

TUNEL Assay

The paraffin-embedded tumor sections were subjected to immunofluorescent labeling. Tumor apoptosis was detected according to the TdT-dependent dUTP-biotin nick labeling (TUNEL) method following the instructions of the assay kit manufacturer (Beyotime Biotechnology Co., Ltd., China). Xylene and gradient alcohol washes were used to remove paraffin from the sections, and then the sections were fixed with 4% formaldehyde. This was followed by tissue labeling using cell nuclear staining solution Hoechst 33,258 and apoptosis indicator. The sections were washed with PBS to remove the background before observation under an orthogonal fluorescence microscope (Zeiss, Germany).

Statistical Analysis

All data including cellular and animal in vivo studies were shown as mean± standard deviation. And the significance between two groups of the data in this work was analyzed on the basis of Student's two-tailed *t*-test (*$p < 0.05$; **$p < 0.01$; ***$p < 0.001$).

Results

Preparation and Characterization of ICG-PEI@HM

ICG-PEI@HM was synthesized by a two-step method (Figure 1). Firstly, the cationic polymer polyethyleneimine (PEI) and ICG were adsorbed into nano-core ICG-PEI particles through electron affinity. Then these were fused with tumor cell membrane using mechanical extrusion method to obtain the biofilm coated nanoplatform ICG-PEI@HM. Different from the intense chemical reactions, the preparation of ICG-PEI@HM was gentle in this study. It was convenient and suitable for in vivo studies. Physical effects guided the entire synthesis process. In particular, the adsorption of PEI to ICG depended on van der Waals force interactions between point charges.[17,18] PEI determines the pH-controlled release of nanomaterials in response to decreasing pH,[19,20] where free protons and acid roots interact with the PEI amino groups competing with ICG in turn causing drug release (Figure 2A). Tightly bound conformational relationships were maintained between ICG, PEI and the cell membrane in a neutral environment. The weak acidic environment touched off the separation of PEI and ICG from the structure. As a result, the structure between the nano-components becomes loose, leading to an increase in the particle size of the nanomaterial.[21] The morphology (including size) of the NPs was characterized by TEM. Under weakly acidic conditions, NPs were diffuse spherical and larger in size than those under neutral conditions (Figure 2B). After ICG coupling, ICG-PEI@HM exhibited rich optical characteristics. As shown in

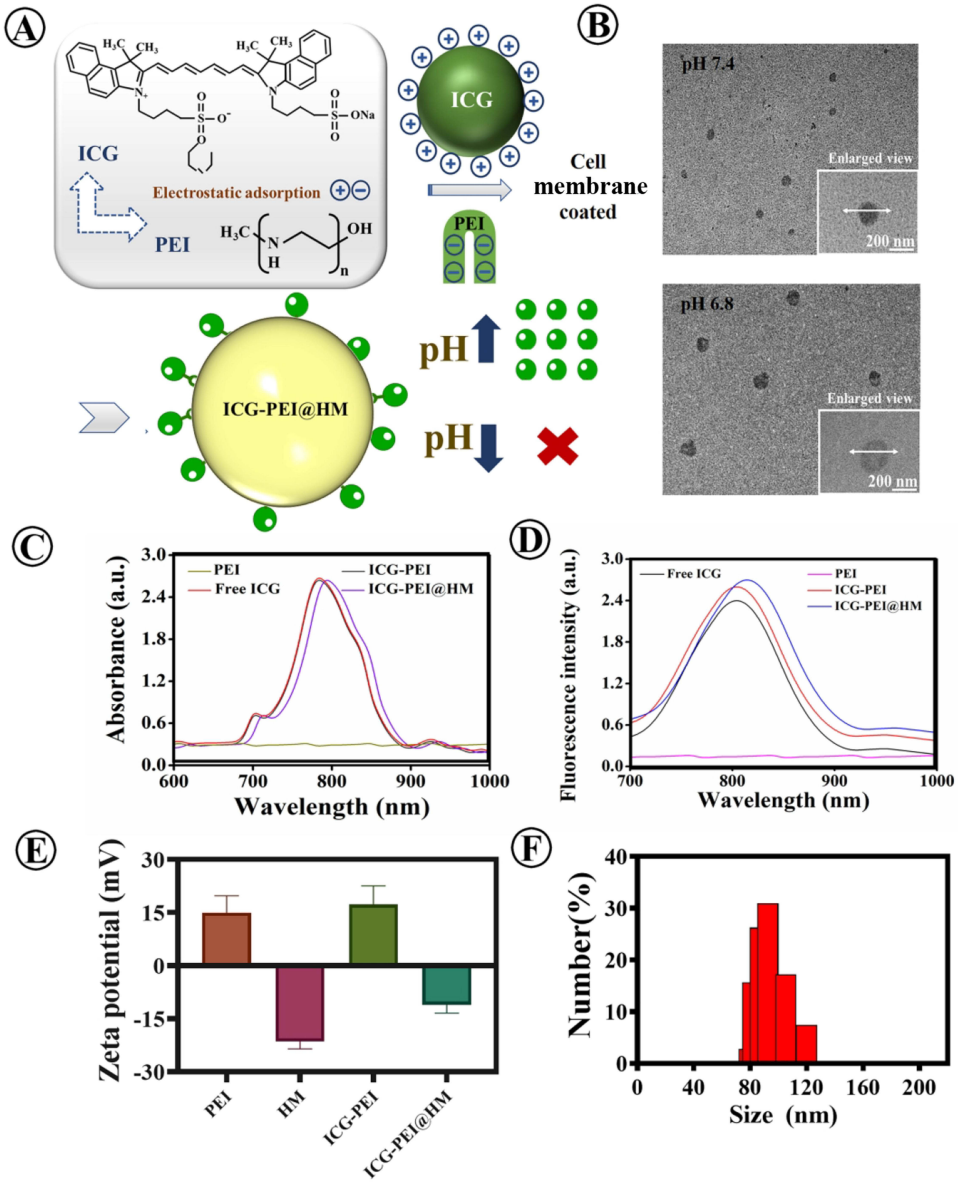

Figure 2 Characterization of ICG-PEI@HM NPs. (**A**) Schematic diagram of the pH responsiveness of ICG-PEI@HM NPs. (**B**) TEM images of ICG-PEI@HM NPs in different pH conditions (bar=200 nm). (**C** and **D**) UV-vis and fluorescence emission spectra of PEI, Free ICG, ICG-PEI, and ICG-PEI@HM NPs. (**E** and **F**) The zeta potential and particle size of ICG-PEI@HM NPs.

Figure 2C and D, compared with free ICG, the absorption and emission peaks of ICG-PEI@HM showed a red-shift due to tight binding within polymer atomic groups. The characteristic excitation and emission peaks were observed at 798 and 830 nm, respectively. In addition, ICG-PEI particles without cell membrane modification were positive potential, while ICG-PEI@HM showed great stability with an electric potential of −11 mV at RT (Figure 2E) and the particle size of 92.5 nm (Figure 2F). During the 30 days monitoring period, the average particle size of ICG-PEI@HM was 94.4 nm in deionized water (Figure 3A). However, the average particle size dispersed in PBS buffer was 95.2 nm (Supplementary Figure 1). There were insignificant changes in ICG-PEI@HM NPs in different media indicated without significant ICG leakage. The colloidal investigation of ICG-PEI@HM NPs with increasing incubation time at a constant temperature of 55°C revealed an insignificant change in particle size suggesting great thermal stability in 90 min (Figure 3B). Although the particle size increased when the incubation time was extended to 240 min, the stability of ICG-PEI@HM could meet the experimental requirements with a relatively short laser irradiation time during the study. ICG release from ICG-PEI @HM NPs was calculated by standard curves to accelerate with decreasing pH (Figure 3C and D), reaching up to

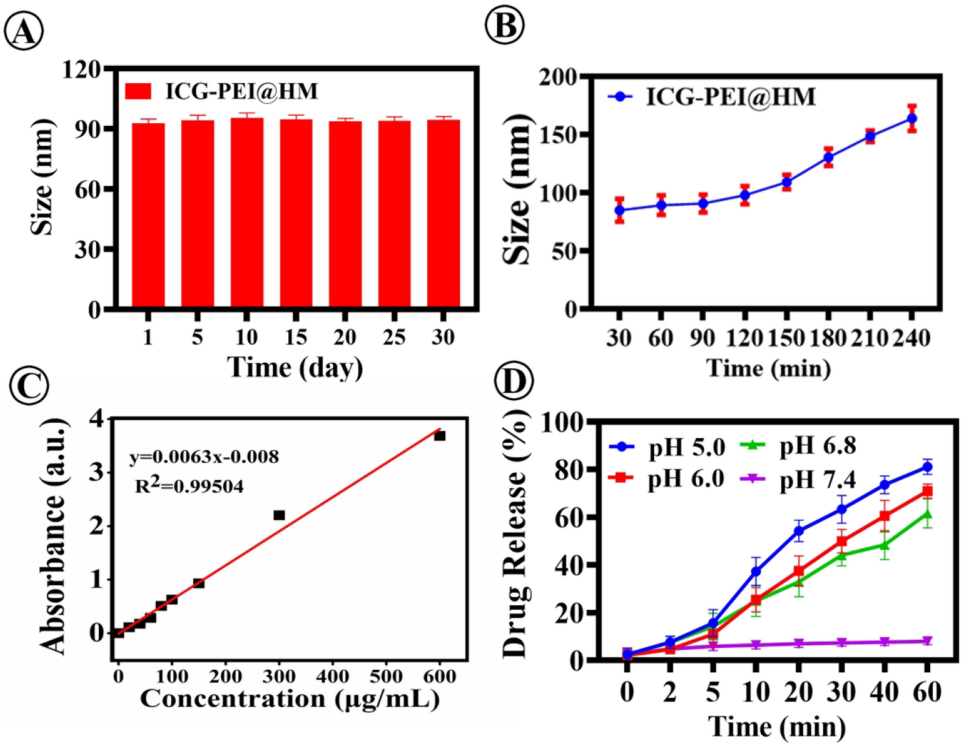

Figure 3 Stability and pH-controlled release performance analysis of ICG-PEI@HM NPs. (**A** and **B**) Colloidal stability and thermal stability of ICG-PEI@HM nanoparticles. (**C**) Standard curve of ICG. (**D**) Controlled release ability of ICG by different pH conditions.

81.36% at pH 5.0 (60 min), and >61.62% in 60 min under weakly acidic conditions (pH 6.8; simulation of tumor environment). These results are consistent with Figure 2A. Overall, ICG-PEI@HM NPs exhibited intelligent pH-responsive drug release and high photothermal therapeutic potential.

Photothermal Performance of Particles

Photothermal performance is the key factor determining the efficacy of tumor therapy. Here, we firstly examined the photothermal conversion properties of ICG-PEI@HM NPs. ICG strongly absorbs the laser light in the near-infrared region to exhibit a photothermal effect.[22] The free ICG has a fixed laser absorption band, while the combination of polymer and membrane protein increases the laser absorption unit of the material.[23] As shown in Figure 4A, after irradiation with 808 nm laser, the temperature of ICG-PEI@HM NPs increased rapidly up to 39°C within 600 s (Tmax >50°C, higher than the threshold for tumor cell killing by PTT) with a photothermal conversion efficiency (η) of 47.18% (η was calculated by the Method). Comparatively, for the same irradiation time range, the free ICG temperature increased up to only 32°C, while the temperature of PEI did not increase. This also corresponds to the NIR image shown in Figure 4C. Compared with previously reported photothermal materials, our ICG-PEI@HM NPs look highly advantageous for photothermal treatment. Moreover, the photothermal capacity of ICG-PEI@HM NPs is positively correlated with laser power (Figure 4B); the temperature of the irradiated ICG-PEI@HM NPs increased with laser power exceeding 65°C after 10 min of irradiation with 1.5 W/cm^2. With the laser (1 W/cm^2, 10 min) irradiation in on/off mode, the thermal conversion ability of the NPs could be cycled continuously indicating its stable photothermal performance (Figure 4D).

Cellular Uptake and ROS Levels

Cellular uptake of the drug secured the photothermal performance.[24,25] Next, NPs incubated with different cell lines (bEnd.3, SW1990, C6, 4T1, and H1975 cells; 4 h) showed the highest fluorescence intensity of ICG (Figure 5A) in H1975 cell lines. And we also investigated the uptake of ICG-PEI particles (without cell membrane) by tumor cells.

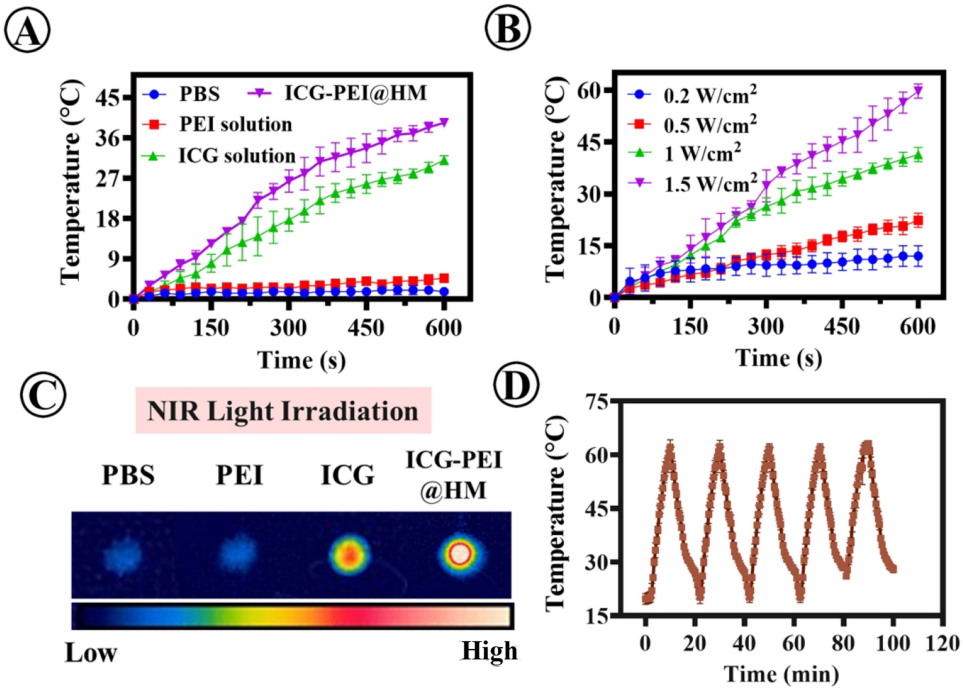

Figure 4 Photothermal conversion data. (**A**) The photothermal profiles of PBS, PEI, ICG, and ICG-PEI@HM NPs. (**B**) Temperature changes of ICG-PEI@HM NPs under different power density irradiations. (**C**) NIR thermal images of samples under laser irradiation. (**D**) The photothermal capability of ICG-PEI@HM NPs over five laser on/off cycles (808 nm, 1 W /cm^2).

When H1975 cells incubated nanoparticles for 12 h, the intracellular ICG red fluorescence was weaker in the ICG- PEI group than in the ICG-PEI@HM NPs group (Supplementary Figure 2A). The flow cytometry quantification results (Supplementary Figure 2B) were consistent with the fluorescence images. Tumor cell membranes have homologous targeting due to the integrin protein family.[26] These results suggest that cell membrane bionic coating improved active targeting of ICG-PEI@HM to enhance drug utilization. Moreover, the effect of different pH environments was evaluated on cellular uptake. Intracellular fluorescence intensity of H1975 cells was monitored by laser confocal microscopy (Figure 5B). The ICG fluorescence intensity increased with incubation time showing an increased red fluorescence on the cell membrane. This can be attributed to the rapid cellular uptake of ICG as a small lipophilic molecule by passive diffusion. Once the pH of the culture environment was reduced from 7.4 to 6.8 (the tumor microenvironment is weakly acidic), the fluorescence intensity of intracellular ICG increased significantly in a time-dependent manner. Flow cytometry data revealed that the cellular uptake of ICG-PEI@HM NPs exhibited a significant pH response (Figure 5C).

ROS levels were positively correlated with PTA's concentration. Herein, the ICG-PEI@HM induced extracellular ROS production was examined using SOSG as a singlet oxygen trap. We found that compared to the light alone group, the level of singlet oxygen produced by ICG-PEI@HM was significantly higher at different laser intensities (Figure 6A and B). DCFH-DA was further examined for intracellular ROS production as a free radical sensor (Figure 6C). The fluorescence images showed a weak green fluorescence signal in the laser-irradiated or ICG-PEI@HM alone groups. This suggested an insignificant amount of cellular ROS. ICG-PEI irradiated at 808 nm produced some ROS due to passive diffusion of certain ICG in the cells, while in the ICG-PEI@HM+Laser group, the active targeting for tumor cells produced a large amount of ROS in response to the tumor pH environment. Therefore, the promoted drug uptake in the ICG-PEI@HM+Laser group showed the strongest green fluorescence. Similar results were obtained by flow cytometry (Figure 6D). The fluorescence intensity in the ICG-PEI@HM+Laser group was 1.38 times higher than the ICG-PEI +Laser group. Afterward, we employed DCFH-DA to capture the ROS generated after laser irradiation at the tissue level which reflected the photothermal effect of ICG-PEI@HM NPs. The free ICG accumulation at the target site was limited because free ICG were not actively targeted. As shown in Supplementary Figure 3, when irradiated with the 808 nm laser, tumor sections from the pH 6.8 group of mice showed high green fluorescence intensity (ROS), while those from

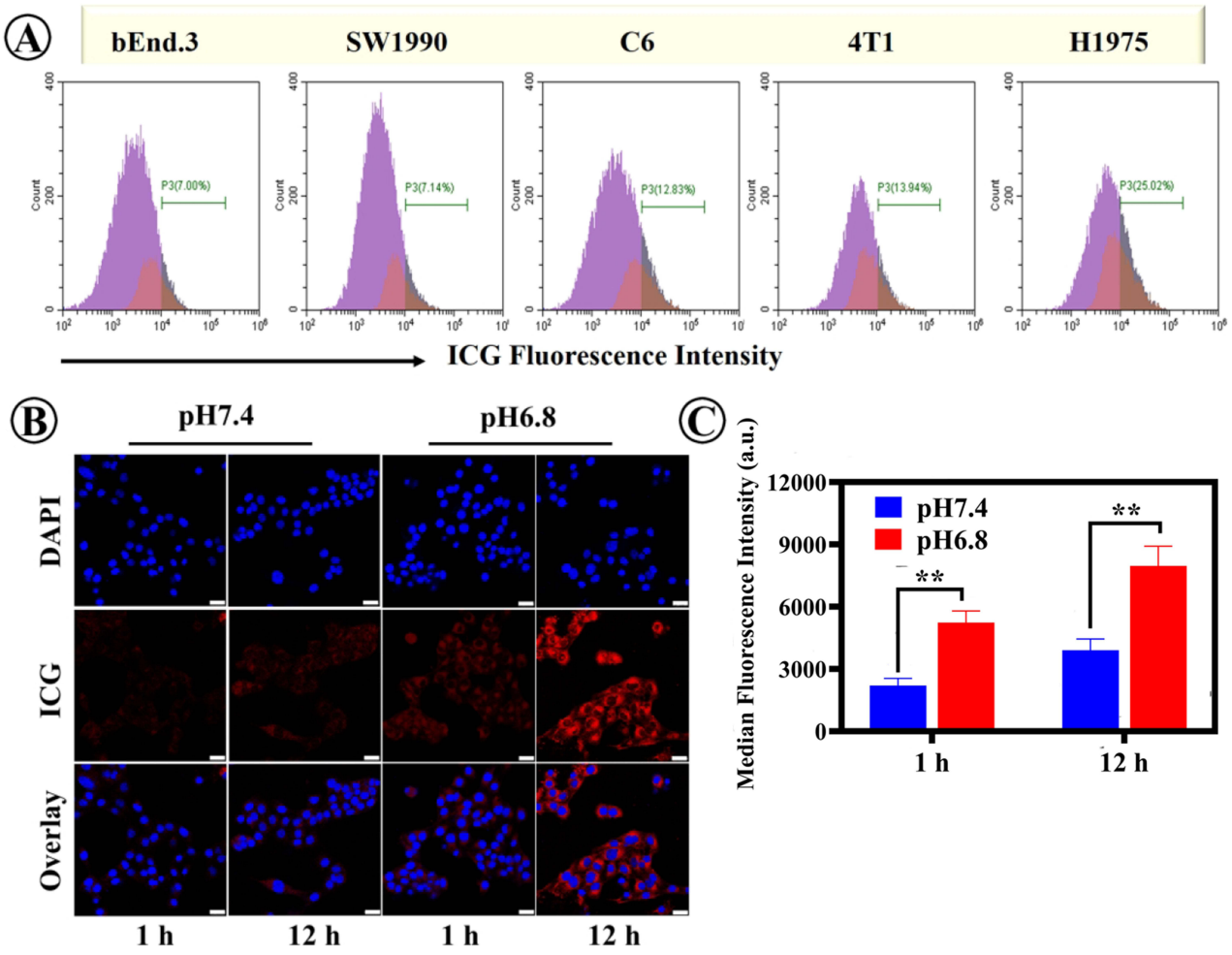

Figure 5 Cellular uptake of ICG-PEI@HM NPs. (**A**) Flow cytometry analysis of Bend.3, SW1990, C6, 4T1, and H1975 cells treated with ICG-PEI@HM NPs (5 μg/mL). (**B** and **C**) CLSM images of the cellular uptake of ICG-PEI@HM NPs and corresponding flow cytometry analysis. The scale bar is 25 μm., $^{**}p<0.01$.
Abbreviations: DAPI, 4',6-diamidino-2-phenylindole; FITC, Fluorescein isothiocyanate.

the pH 7.4 group showed relatively weak fluorescence. Combined with Figure 5B, it can be seen that more nanoparticles were accumulated in the weak acid group compared to the neutral group. Therefore, the ICG-PEI@HM NPs produced more ROS after laser irradiation. In brief, the above results suggest that ICG-PEI@HM NPs possess a stronger ability to produce ROS. The tumor cell membrane coating improved active targeting but did not affect the ROS generation. This rather improved the biocompatibility, PTT performance, and therapeutic efficacy of the nanomaterial.

Cytotoxicity

The potential cytotoxicity of ICG-PEI@HM NPs was evaluated by the MTT method on NIH 3T3 and H1975 cells. Supplementary Figure 4 shows the cell survival rate for different drug concentrations. There was almost no cytotoxicity up to 160 μg/mL drug concentrations with >80% viability of NIH3T3 cells suggesting excellent safety. Besides, we examined the effect of different treatment parameters on cell viability. In Supplementary Figure 5, H1975 cells were treated with low doses of ICG-PEI@HM NPs. The aim of this experiment was to screen subsequent treatment parameters and to highlight the advantages of combining drugs with light irradiation. This study found that with an increase in laser irradiation power, the cell viability of H1975 decreased; at 1 W/cm^2 irradiation, the cell viability was <80% (Supplementary Figure 6). The drug was biocompatible and was found relatively safe up to 5 μg/mL (Supplementary Figure 5). In addition, 808 nm laser irradiation (1 W/cm^2, 10 min) combined ICG-PEI@HM NPs decreased the cell viability significantly (18%) and the cytotoxicity showed a laser power-dependence (Supplementary Figure 7).

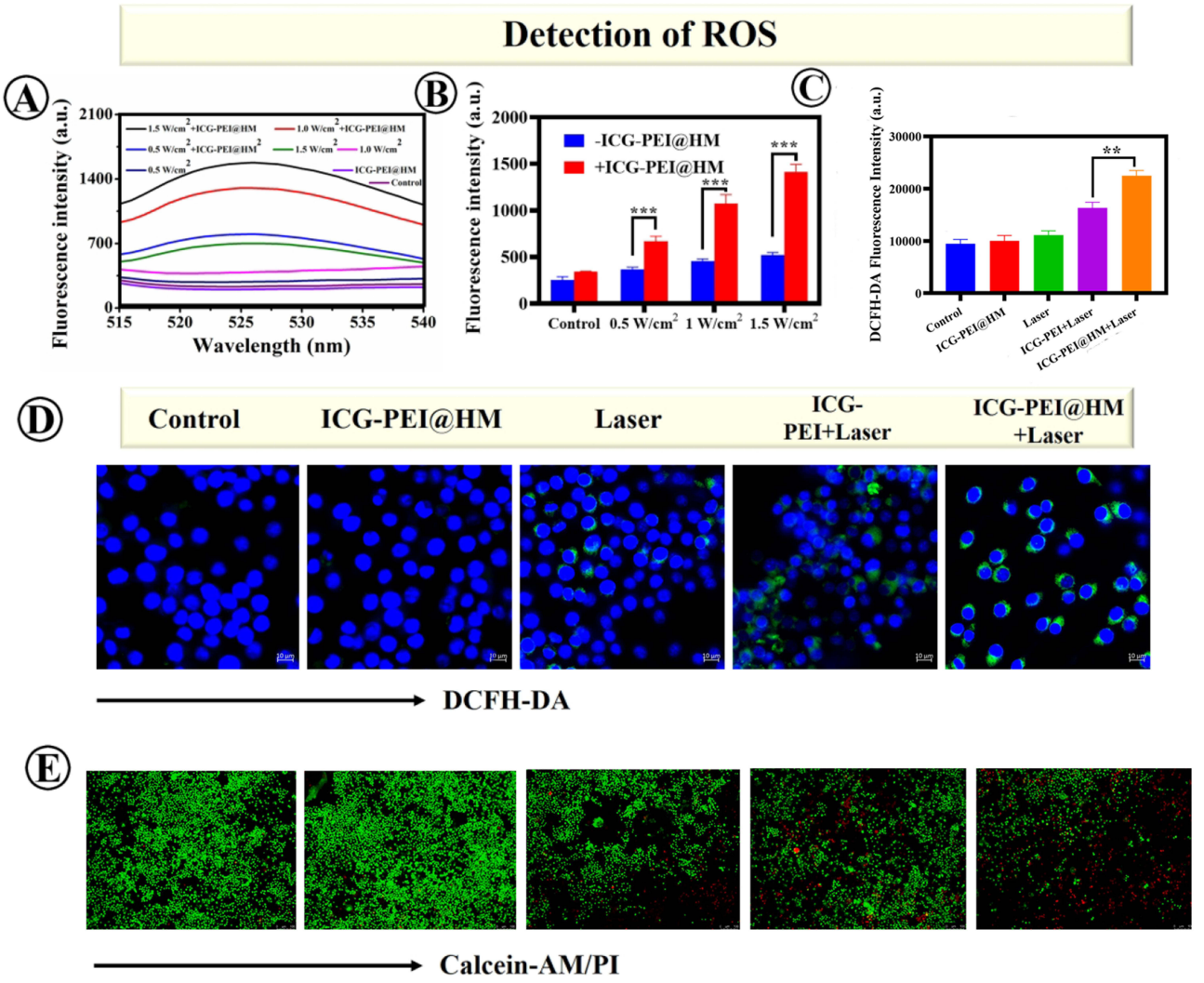

Figure 6 ICG-PEI@HM nanoparticles-mediated PTT therapy-induced ROS generation and cytotoxicity studies. (**A** and **B**) The generated single oxygen of ICG-PEI@HM NPs under different irradiations conditions (808 nm, 10 min) using SOSG probe. (**C** and **D**) Fluorescence images and flow cytometry quantification of intracellular DCFH-DA. $^{**}p<0.01$, $^{***}p<0.001$. (**E**) Calcein-AM and PI staining of H1975 cells after different treatments (the concentration of ICG-PEI and ICG-PEI@HM was equivalent to 5 μg/mL ICG, green: Calcein-AM, red: PI). The scale bar is 250 μm.

Abbreviations: ROS, Reactive oxygen species; DCFH-DA, 2′,7′-dichlorofluorescin diacetate.

To visually evaluate the photothermal treatment performance of ICG-PEI@HM at the cellular level, we labeled live and dead cells by Calcein-AM and PI, respectively (Figure 6E). The strongest intensity of PI-red fluorescence was observed in the ICG-PEI@HM+Laser group (5 μg/mL, 1 W/cm^2, 10 min). The fewer red fluorescence signals were also observed in the ICG-PEI+Laser group, the strong green fluorescence indicated a higher number of live cells. This result can be attributed to the active targeting ability of the bionic membrane layer and the excellent photothermal properties of the composite material; both of which enhanced the PTT effect.

In vivo Imaging and Drug Penetration

To study the biodistribution behavior in vivo, ICG-PEI@HM NPs were injected into mice via tail vein. A weak fluorescence enrichment of free ICG was observed at the mice tumor site 3 h after injection (Figure 7A). The fluorescence intensity was higher in the ICG-PEI group than in the free ICG group, suggesting ICG-containing nanoparticles could be effectively concentrated at tumor site. With the increase in cycling time, the fluorescence intensity in the ICG-PEI@HM NPs group increased significantly higher due to the active targeting than the other two groups. Furthermore, ICG-PEI@HM NPs showed great pH-controlled release ability at different tissue acidity levels. The red

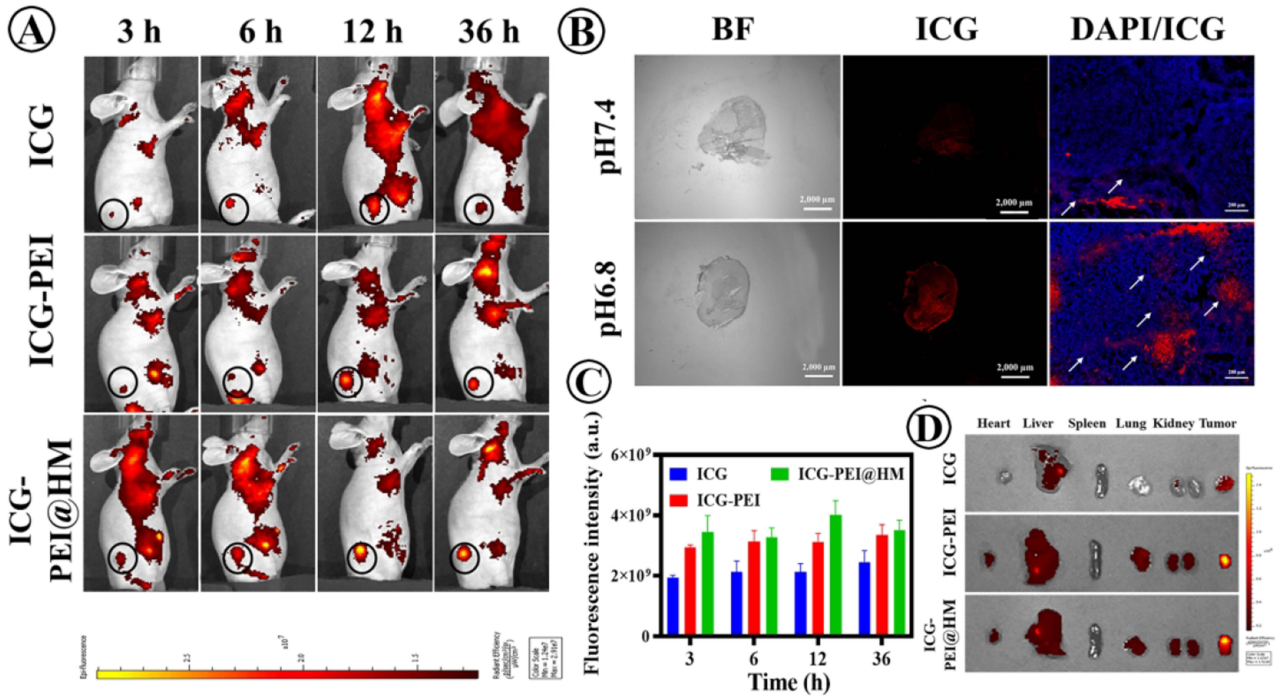

Figure 7 In vivo fluorescence imaging and tissue distribution. (**A**) In vivo optical images of H1975 tumor-bearing mice observed at different time points after intravenous injection of free ICG and ICG-PEI@HM NPs. (**B**) Penetration of ICG-PEI@HM NPs in vivo tumor tissues. The scale bar is 2000 μm. (**C** and **D**) Time-dependent averaged fluorescence intensity of ICG fluorescence at the tumor site post intravenous injection and drug distribution in the organs of each group of mice.

fluorescence of ICG increased with decreasing pH of tumor tissue (Figure 7B), while free ICG exhibited weaker fluorescence. The quantitative results shown in Figure 7C are consistent with the results of fluorescence imaging; the fluorescence intensity in mouse tumors reached the highest at 12 h. ICG-PEI@HM NPs showed fluorescence signals after 36 h of injection, and the longer blood circulation ensured the effective accumulation at tumor sites. For further investigation, the main organs of the mice were removed. The study detected only a weak fluorescence of NPs in metabolic organs such as the liver and kidney, while the tumor tissues showed the highest fluorescence intensity (Figure 7D). This strongly suggests excellent tumor targeting of these nanomaterials.

In vivo PTT

H1975 tumor-bearing mice were further used to assess the photothermal antitumor efficacy of ICG-PEI@HM NPs in vivo (Figure 8A). The tumor-bearing mice were equally assigned to each group for the respective treatment. During the monitoring period, the tumor volume of mice in the Control and ICG-PEI@HM NPs groups continued to grow (Figure 8B and C). Although the tumor suppression in the ICG+Laser (17.79%) and ICG-PEI+Laser (45.75%) groups was not much effective, it was still higher than in the unirradiated group (Figure 8D). Among all the groups, the ICG-PEI @HM+Laser group showed maximum tumor suppression (90.49%) which is consistent with the results of in vivo imaging (Supplementary Figure 8). Moreover, the subcutaneous tumors almost disappeared at day 21 suggesting a better effect of PTT. Histopathological examination revealed a larger area of tissue damage and sparse cell interstices in the ICG-PEI@HM+Laser group than in the ICG-PEI+Laser group. Notably, TdT-dependent dUTP-biotin nick labeling (TUNEL) validated ICG-PEI@HM+Laser-induced apoptosis.[27] The ICG-PEI+Laser and ICG-PEI@HM+Laser groups showed significant tumor cell apoptosis (Figure 8F). The strongest green apoptotic signal in the latter group showed a clear advantage of ICG-PEI@HM+Laser in treating H1975 tumors.

Biosafety of ICG-PEI@HM

In this study, we not only evaluated the efficacy but also examined the biosafety of the treatment for the ICG-mediated PTT treatment modality. The safety of the treatment modality has potentially translational clinical implications. Firstly,

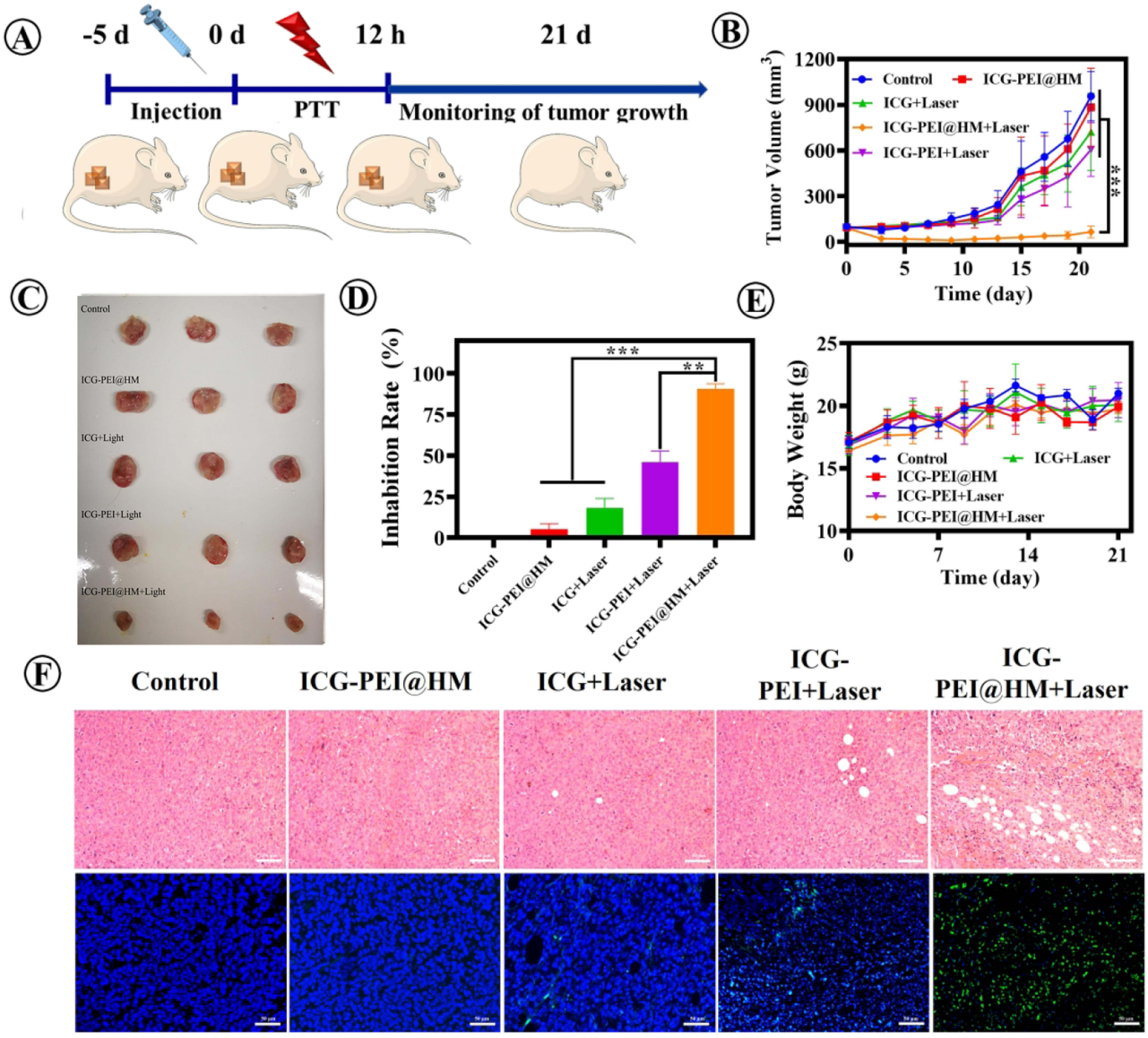

Figure 8 Photothermal antitumor applications and histochemical data. (**A**) Schematic diagram of in vivo photothermal treatment in H1975 tumor-bearing mice. (**B** and **C**) Tumor volume and morphology of mice at day 21 after different treatments (n = 9). (**D**) Tumor-inhibition rate of H1975 tumor-bearing mice after different treatments., $^{**}p<0.01$, $^{***}p<0.001$. (**E**) Body weight of the mice after various treatments. (**F**) Tumor histochemical analysis (upper row: H&E, lower row: TUNEL, scale bar: 50 μm).
Abbreviations: TUNEL, TdT-dependent dUTP-biotin nick labeling; H&E, Hematoxylin-eosin staining.

the changes in body weight showed no statistically significant difference among the ICG-PEI@HM+Laser, Control, and ICG-PEI@HM groups (Figure 8E) suggesting no effect on mice growth. Furthermore, compared with the Normal group (without tumor), pathological analysis (H&E staining) showed no pathological enlargement in the alveolar cavity or congestion in the alveolar interstitial vessels[28] in the ICG-PEI@HM+Laser group. Also, no significant damages were noticed in other major organs including the heart, liver, spleen, and kidney (Supplementary Figure 9). The clear structure of nucleus, homogeneous cytoplasmic staining and no obvious cell necrosis were observed, indicating that the treatment mode was virtually free of toxic side effects and toxicity to these organs, further highlighting its superior biosafety. The serum levels of alanine aminotransferase (ALT), blood urea nitrogen (BUN) and aspartate aminotransferase (AST) in the mice mainly reflected the liver and kidney function of the mice (Supplementary Figure 10). Although the main blood biochemical parameters decreased compared to normal mice, these parameters were still within the normal range, suggesting that the metabolic system of the mice was stable.[29] It was considered that there were factors such as

environmental and individual variability during the experimental treatment. In conclusion, these results demonstrated the safety of ICG-PEI@HM NPs.

Discussion

Herein, the pH-responsive bionic nanoplatform ICG-PEI@HM was designed to promote ICG accumulation at the tumor target site to enhance the efficacy of PTT. The tumor-bearing mice avoided multiple photothermal irradiations, and only one dose of injection combined with laser irradiation effectively inhibited the tumor growth. However, the tumor was not fully eradicated. The lung adenocarcinoma cell line easily developed resistance to limit the therapeutic effect of conventional therapy,[30] where epidermal growth factor receptors (EGFR) were positively correlated with tumor treatment resistance. The pH responsiveness based on ICG-PEI@HM can be observed in the tissue sections in this study, and PTA was effectively tissue penetrated, further suggesting the relevance of the bionic targeting strategy with EFGR. Several recent studies demonstrated the great potential of individualized molecular targeting strategies for the treatment of non-small cell lung cancer.[31] Especially, a study showed the epidermal growth factor receptor (EGFR) and mesenchymal lymphoma kinase as targeted drugs for the development of individualized tumor therapy.[32] To integrate the advantages of multimodal therapy, many studies examined synergistic PDT and sonodynamic for targeted tumor therapy. The synergistic strategy of PTT combined with targeting has shown better therapeutic efficacy. In 2019, Feng et al designed a gold nanocage carrying the EGFR inhibitor erlotinib (ERl) and the chemotherapeutic agent DOX that produced cascade-controlled drug release for optimal photochemotherapy. Based on the ERl mediated targeting, the designed nanocage achieved a higher killing rate of EGFR over-expressing squamous cells.[33] Combining multiple therapies based on ERl can potentiate anti-tumor effects. In addition, a combination of ERl and DOX reduced the required dose of chemotherapeutic agents reducing side effects. Also, the synergistic effect of the combination therapy can reverse cellular drug resistance enhancing the anti-tumor efficacy.[34] In addition, PTT can promote the ICG release from the ICG-PEI@HM nanoparticles, as much high heat breaks the interaction between PEI and ICG.

Likewise, the integration of nano diagnosis and therapy is gaining wider attention. The ICG-PEI@HM NPs demonstrated the fluorescence tracer performance in vivo for ICG delivery. Optical imaging is a widely used clinical practice for its low cost and ease of operation. The current development of multimodal imaging has overcome the issue of tissue barrier; also, the lasers of different wavelengths have greatly improved the imaging resolution. Near-infrared second region imaging (1000–1700 nm, NIR-II) overcame the problem of strong tissue absorption, scattering, and achieved higher tissue penetration and spatial resolution for in vivo imaging.[35] The imaging system is considered the most promising next-generation in vivo fluorescence imaging technology.[36] ICG is compatible with several NIR imaging windows and lays the foundation for excellent imaging.[21] Suo et al proposed to use ICG to design a NIR-II -internal abscopal endoscopic imaging technique to study structural morphology and molecular characteristics of diseases in real-time. This system can achieve better accuracy for the imaging of many tumors and similar diseases.[37] For instance, the expansion of nanomedicine for NIR-II imaging can help navigate the tumor target site examining the complex morphology of tumor vasculature. Such a novel biomedical strategy establishes an absolute advantage in antitumor diagnosis.

Conclusion and Future Perspective

In this study, a pH-responsive bionic smart nanoplatform was successfully developed by loading tumor cell membranes with ICG adsorbed with PEI. H1975 cell membranes determine the targeting, while PEI controls the pH-based release of ICG. ICG-PEI@HM NPs exhibited excellent thermal stability and pH responsiveness. More importantly, the NPs showed better photothermal performance and stable thermal conversion capacity for sustainable cycling. Besides, the NPs have been shown great biocompatibility with limited cytotoxicity. Laser irradiation combined with NPs effectively reduced the cell viability and increased the efficacy of PTT. And ICG-PEI@HM NPs mediated-PTT therapy significantly inhibited tumor growth in vivo. An intelligent targeted nanodrug delivery system, such as ICG-PEI@HM, can effectively enhance the drug accumulation at the target site. Moreover, fluorescence imaging-guided photothermal therapy can be more precise, as well it provides a novel strategy for the construction of a visual PTAs.

Ethical Conduct of Research

Nude male BALB/c mice (4–6 weeks old, weighing 14–21 g) were purchased from Jining Medical University (Jining, China). The authors state that all animal experiments were done according to the protocol sanctioned by the Animal Care and Use Committee of Jining No. 1 People's Hospital. All experiments and animals care were conducted in accordance with the Provision and General Recommendation of Chinese Experimental Animals Administration Legislation and were approved by the Science Department of Jining No. 1 People's Hospital (No. 2018-RM-002).

Author Contributions

All authors made a significant contribution to the work reported, whether that is in the conception, study design, execution, acquisition of data, analysis and interpretation, or in all these areas; took part in drafting, revising or critically reviewing the article; gave final approval of the version to be published; have agreed on the journal to which the article has been submitted; and agree to be accountable for all aspects of the work.

Funding

This work was supported by the National Natural Science Foundation of China (Grant No. 81803097), the Natural Science Foundation of Shandong Province (Nos. ZR2023MH260 and ZR2017QH005), Doctoral Fund of Jining No.1 People's Hospital (2022-BS-002) and Key R&D Program of Jining (2022YXNS113).

Disclosure

The authors report no conflicts of interest in this work.

References

1. Cheng L, Wang C, Feng L, et al. Functional nanomaterials for phototherapies of cancer. *Chem Rev*. 2014;114(21):10869–10939. doi:10.1021/cr400532z
2. Jaque D, Martinez ML, Del Rosal B, et al. Nanoparticles for photothermal therapies. *Nanoscale*. 2014;6(16):9494–9530. doi:10.1039/C4NR00708E
3. Han X, Huang J, Jing X, et al. Oxygen-deficient black titania for synergistic/enhanced sonodynamic and photoinduced cancer therapy at near infrared-II biowindow. *ACS Nano*. 2018;12(5):4545–4555. doi:10.1021/acsnano.8b00899
4. Dolmans DE, Fukumura D, Jain RK. Photodynamic therapy for cancer. *Nat Rev Cancer*. 2003;3(5):380–387. doi:10.1038/nrc1071
5. Aioub M, Panikkanvalappil SR, El-Sayed MA. Platinum-coated gold nanorods: efficient reactive oxygen scavengers that prevent oxidative damage toward healthy, untreated cells during plasmonic photothermal therapy. *ACS Nano*. 2017;11(1):579–586. doi:10.1021/acsnano.6b06651
6. Liu H, Chen D, Li L, et al. Multifunctional gold nanoshells on silica nanorattles: a platform for the combination of photothermal therapy and chemotherapy with low systemic toxicity. *Angew Chem Int Ed Engl*. 2011;50(4):891–895. doi:10.1002/anie.201002820
7. Sun X, Guo L, Shang M, et al. Ultrasound mediated destruction of LMW-HA-loaded and folate-conjugated nanobubble for TAM targeting and reeducation. *Int J Nanomedicine*. 2020;15:1967–1981. doi:10.2147/IJN.S238587
8. Fang RH, Kroll AV, Gao W, Zhang L. Cell membrane coating nanotechnology. *Adv Mater*. 2018;30(23):e1706759. doi:10.1002/adma.201706759
9. Li C, Yang X, An J, et al. Red blood cell membrane-enveloped O_2 self-supplementing biomimetic nanoparticles for tumor imaging-guided enhanced sonodynamic therapy. *Theranostics*. 2020;10(2):867–879. doi:10.7150/thno.37930
10. Geng X, Gao D, Hu D, et al. Active-targeting NIR-II phototheranostics in multiple tumor models using platelet-camouflaged nanoprobes. *ACS Appl Mater Interfaces*. 2020;12(50):55624–55637. doi:10.1021/acsami.0c16872
11. Egloff-Juras C, Bezdetnaya L, Dolivet G, Lassalle HP. NIR fluorescence-guided tumor surgery: new strategies for the use of indocyanine green. *Int J Nanomedicine*. 2019;14:7823–7838. doi:10.2147/IJN.S207486
12. Esposito C, Settimi A, Del Conte F, et al. Image-guided pediatric surgery using indocyanine Green (ICG) fluorescence in laparoscopic and robotic surgery. *Front Pediatr*. 2020;8:314. doi:10.3389/fped.2020.00314
13. Zhou J, Meng L, Sun C, et al. A "protective umbrella" nanoplatform for loading ICG and multi-modal imaging-guided phototherapy. *Nanomedicine*. 2018;14(2):289–301. doi:10.1016/j.nano.2017.09.009
14. Luo Z, Tian H, Liu L, et al. Tumor-targeted hybrid protein oxygen carrier to simultaneously enhance hypoxia-dampened chemotherapy and photodynamic therapy at a single dose. *Theranostics*. 2018;8(13):3584–3596. doi:10.7150/thno.25409
15. Wang Y, Luo S, Wu Y, et al. Highly penetrable and on-demand oxygen release with tumor activity composite nanosystem for photothermal/photodynamic synergetic therapy. *ACS Nano*. 2020;14(12):17046–17062. doi:10.1021/acsnano.0c06415
16. Liu Y, Zhang D, Qiao Z, et al. A peptide-network weaved nanoplatform with tumor microenvironment responsiveness and deep tissue penetration capability for cancer therapy. *Adv Mater*. 2015;27(34):5034–5042. doi:10.1002/adma.201501502
17. Davood A, Alexander K, Naresh BK, et al. Electron trapping in conjugated polymers. *Chem Mater*. 2019;31:6380–6386.
18. Kirill AE, Alexandre ME, Ludmila BB. Van der Waals forces in free and wetting liquid films. *Adv. Colloid Interface Sci*. 2019;269:357–369. doi:10.1016/j.cis.2019.04.013
19. Guan X, Guo Z, Lin L, et al. Ultrasensitive pH Triggered Charge/Size dual-rebound gene delivery system. *Nano Lett*. 2016;16(11):6823–6831. doi:10.1021/acs.nanolett.6b02536

20. Lei Q, Wang S, Hu J, et al. Stimuli-responsive "cluster bomb" for programmed tumor therapy. *ACS Nano*. 2017;11(7):7201–7214. doi:10.1021/acsnano.7b03088
21. Jun S, Wei Y, Hu J, et al. pH-Responsive porous nanocapsules for controlled release. *Chem Eur J*. 2018;24(1):212–221. doi:10.1002/chem.201704328
22. Campu A, Focsan M, Lerouge F, et al. ICG-loaded gold nano-bipyramids with NIR activatable dual PTT-PDT therapeutic potential in melanoma cells. *Colloids Surf B Biointerfaces*. 2020;194:111213. doi:10.1016/j.colsurfb.2020.111213
23. Paul S, Heng PW, Chan LW. pH-dependent complexation of hydroxypropyl-beta-cyclodextrin with chlorin e6: effect on solubility and aggregation in relation to photodynamic efficacy. *J Pharm Pharmacol*. 2016;68(4):439–449. doi:10.1111/jphp.12535
24. Adjei IM, Sharma B, Labhasetwar V. Nanoparticles: cellular uptake and cytotoxicity. *Adv Exp Med Biol*. 2014;811:73–91.
25. Jiang Q, Liu Y, Guo R, et al. Erythrocyte-cancer hybrid membrane-camouflaged melanin nanoparticles for enhancing photothermal therapy efficacy in tumors. *Biomaterials*. 2019;192:292–308. doi:10.1016/j.biomaterials.2018.11.021
26. Wu PH, Abayomi EO, Yasuhito O, et al. Targeting integrins in cancer nanomedicine: applications in cancer diagnosis and therapy. *Cancers*. 2019;11(11):1783. doi:10.3390/cancers11111783
27. Short B. TUNEL vision spots apoptotic cells. *J Cell Biol*. 2015;208(1):7. doi:10.1083/jcb.2081fta
28. Bernardi FD, Bernardi MD, Takagaki T, et al. Lung cancer biopsy: can diagnosis be changed after immunohistochemistry when the H&E-Based morphology corresponds to a specific tumor subtype? *Clinics*. 2018;73:e361. doi:10.6061/clinics/2018/e361
29. Xuan Y, Zhan R, Zhao D, et al. Ultrafast synthesis of gold nanosphere cluster coated by graphene quantum dot for active targeting PA/CT imaging and near-infrared laser/pH-triggered chemo-photothermal synergistic tumor therapy. *Chem Eng J*. 2019;369:87–99. doi:10.1016/j.cej.2019.03.035
30. Wang Y, Zhu Y, Yip R, et al. Pre-surgical assessment of mediastinal lymph node metastases in Stage IA non-small-cell lung cancers. *Clin Imaging*. 2020;68:61–67. doi:10.1016/j.clinimag.2020.06.016
31. Liu HE, Vuppalapaty M, Wilkerson C, et al. Detection of EGFR Mutations in cfDNA and CTCs, and comparison to tumor tissue in non-small-cell-lung-cancer (NSCLC) patients. *Front Oncol*. 2020;10:572895. doi:10.3389/fonc.2020.572895
32. Mehlman C, Cadranel J, Rousseau-Bussac G, et al. Resistance mechanisms to osimertinib in EGFR-mutated advanced non-small-cell lung cancer: a multicentric retrospective French study. *Lung Cancer*. 2019;137:149–156. doi:10.1016/j.lungcan.2019.09.019
33. Feng Y, Cheng Y, Chang Y, et al. Time-staggered delivery of erlotinib and doxorubicin by gold nanocages with two smart polymers for reprogrammable release and synergistic with photothermal therapy. *Biomaterials*. 2019;217:119327. doi:10.1016/j.biomaterials.2019.119327
34. He Y, Su Z, Xue L, et al. Co-delivery of erlotinib and doxorubicin by pH-sensitive charge conversion nanocarrier for synergistic therapy. *J Control Release*. 2016;229:80–92. doi:10.1016/j.jconrel.2016.03.001
35. Zhu S, Tian R, Antaris AL, et al. Near-Infrared-II molecular dyes for cancer imaging and surgery. *Adv Mater*. 2019;31(24):e1900321. doi:10.1002/adma.201900321
36. Xu G, Yan Q, Lv X, et al. Imaging of colorectal cancers using activatable nanoprobes with second near-infrared window emission. *Angew Chem Int Ed Engl*. 2018;57(14):3626–3630. doi:10.1002/anie.201712528
37. Suo Y, Wu F, Xu P, et al. NIR-II fluorescence endoscopy for targeted imaging of colorectal cancer. *Adv Healthc Mater*. 2019;8(23):e1900974. doi:10.1002/adhm.201900974